Synchrotron-based visualization and segmentation of elastic lamellae in the mouse carotid artery during quasi-static pressure inflation

Bram Trachet, PhD[1,2*], Mauro Ferraro, PhD[1], Goran Lovric, PhD[3,4], Lydia Aslanidou[1], Gerlinde Logghe[2], Patrick Segers, PhD[2] and Nikolaos Stergiopulos, PhD[1]

[1] Institute of Bioengineering, Ecole Polytechnique Fédérale de Lausanne, Lausanne, Switzerland

[2] IBiTech-bioMMeda, Ghent University, Ghent, Belgium

[3] Centre d'Imagerie BioMédicale, École Polytechnique Fédérale de Lausanne, Lausanne, Switzerland

[4] Swiss Light Source, Paul Scherrer Institute, Villigen, Switzerland

* Corresponding author:

Email: bram.trachet@ugent.be

Phone: +41216938342, ORCID-ID: 0000-0003-4863-8399

The authors have no conflicts of interest to declare

Synchrotron-based visualization and segmentation of elastic lamellae in the mouse carotid artery during quasi-static pressure inflation

Bram Trachet, Mauro Ferraro, Goran Lovric, Lydia Aslanidou, Gerlinde Logghe, Patrick Segers, Nikolaos Stergiopulos.

Journal of the Royal Society Interface 2019, 16 (155)

doi: 10.1098/rsif.2019.0179

Abstract

In computational aortic biomechanics aortic and arterial tissue are typically modelled as a homogeneous layer, making abstraction not only of the layered structure of intima, media and adventitia but also of the micro-structure that exists within these layers. Here, we present a novel method to visualize the micro-structure of the tunica media in 3D, along the entire circumference of the vessel. To that end we developed a pressure inflation device that is compatible with synchrotron-based phase contrast imaging. Using freshly excised left common carotid arteries from n=12 mice, we visualized how the lamellae and interlamellar layers inflate as the luminal pressure is increased from 0 to 120 mmHg in quasi-static steps. A graph-based segmentation algorithm subsequently allowed us to automatically segment each of the three lamellae, resulting in a 3D geometry that represents lamellae, interlamellar layers and adventitia at 9 different pressure levels. Our results demonstrate that the three elastic lamellae unfold and stretch simultaneously as luminal pressure is increased. In the long term, we believe that the results presented in this work can be a first step towards a better understanding of the mechanics of the arterial micro-structure.

Keywords: mouse models of cardiovascular disease, aortic lamellae, aortic microstructure, synchrotron-based biomechanics

Introduction

The aorta and its main large proximal branches buffer blood from the heart during systole and propel it downstream during diastole. From a mechanical point of view aortic and arterial tissue behave as a hyperelastic soft tissue at low tensile stresses and strains, while they undergo a characteristic stiffening as stress and strain increase. This phenomenon has been evidenced by uniaxial (1, 2) and biaxial (3-5) tension tests on flattened samples, as well as pressure inflation tests on cylindrical samples (6). As any artery, the large proximal elastic arteries are composite structures that are organized in three distinct layers (tunica intima, media and adventitia). These layers are distinctly different from each other in terms of constituents, mechanical stiffness and ultimate tensile strength (7, 8). On a micro-structural level, the tunica media is composed of smooth muscle cells and collagen fibers that are embedded in a network of concentric elastic lamellae (9-11), while the adventitia is composed of thick collagen bundles that are organized in a network of helically oriented elastic fibers (12). Constitutive models are generally based on a strain energy function in which the arterial wall is modelled as a soft matrix material reinforced by different fiber families (13, 14). The mechanisms that govern the rearrangements of the micro-structure in response to an increase in stress remain, however, largely unexplored (15).

One of the most important factors hampering a thorough understanding of the kinematics and dynamics of the aortic micro-structure is the lack of visualization methods for the structural (re)arrangement of the individual constituents (under loading). The earliest images of the micro-structure of the aorta were obtained with scanning electron microscopy (16) and transmission electron microscopy (10). However, these methods essentially yield 2D images and exclude kinematical studies since they cannot be combined with deformation during physiological loading. Moreover, they suffer from image artifacts caused by the need to chemically digest all collagen fibers prior to imaging the elastin components (or vice versa) (17). Multiphoton microscopy (MPM) allowed researchers to overcome some of these limitations as both elastin and collagen could be visualized

simultaneously without the necessity of tissue-preprocessing. A crucial limitation of MPM, however, is the limited field of view, which restricts the depth of observation in most applications to the adventitial layer (18, 19). MPM-based methods have been developed to visualize the lamellar microstructure within the tunica media in mice, both in the descending aorta (20) and the carotid artery (21), but the field of view did not suffice to visualize the entire circumference of the vessel.

An alternative approach to visualize the aortic micro-structure in 3D and at different pressure levels is to take advantage of synchrotron-based phase contrast imaging (22). In traditional micro-CT, an image is generated by the differential absorption of X-rays that travel through the aorta. In synchrotron-based phase-contrast imaging, on the other hand, images are based on the phase distortions of the X-ray wave fronts that travel through a specimen, which generally allows for a significantly higher signal to noise ratio and an improved spatial resolution (23). When used to visualize the mouse vasculature, synchrotron images typically combine a detailed resolution with a field of view that encompasses the entire circumference of the vessel (22). In recent experiments we used synchrotron-based grating interferometry to visualize ascending (24) and dissecting abdominal aortic aneurysms (25, 26) in mice, while propagation-based phase contrast imaging has been used by us and others to visualize the degeneration of aortic lamellae in aneurysm formation (27, 28).

Here, we decided to take our imaging approach one step further and use synchrotron imaging in order to determine both the geometry and material properties of the arterial micro-structure. To that end we combined synchrotron-based phase propagation imaging with quasi-static pressure inflation experiments on freshly excised carotid arteries from mice. Using a custom-built, synchrotron-compatible pressure inflation tool we demonstrate how the elastic lamellae in the mouse carotid artery unfold with pressure. We also introduce a robust graph-based segmentation algorithm that yields a full 3D description of each of the lamellae within the mouse carotid artery.

Methods

Synchrotron-compatible quasi-static pressure inflation device

A custom-built pressure-inflation device was designed in SolidWorks (Dassault systems, France). Synchrotron-specific design requirements were that during the scans (i) the tissue sample should be placed in a PMMA tube that is transparent for X-rays, (ii) the sample should be held in vertical rather than horizontal position, in order to fit within the field of view of the X-ray beam, (iii) the total vertical length of the entire set-up should be such that the PMMA tube fits within the field of view of the X-ray beam, and (iv) the pressure should be kept constant for several minutes, to allow for sufficient scan time at each quasi-static pressure level. The resulting device was geometrically adapted to fit the requirements of the X02DA TOMCAT beamline at the Swiss Light Source (PSI, Villigen, Switzerland), but in principle it can be adapted to fit any powerful micro-CT device. A syringe pump was used to increase the pressure inside the carotid artery (Figure 1a), which was monitored during the experiment with a pressure sensor (SunX DP-100, Panasonic, Japan). During the experiments the device was fixed with screws on the synchrotron experimental setup (Figure 1b), such that the PMMA tube holding the aortic sample was placed within the X-ray beam (Figure 1c). The sample was mounted in horizontal position using a separate setup (Figure 1d). During the experiment, the mounted sample was placed in vertical position. Liquid tightness was ensured with rubber O-ring seals at both sides of the cylinder. Additional O-rings were placed between cylinder and brass needles (Figure 1e).

Experimental procedure

N=6 male C57BL/6J mice and n=6 male ApoE$^{-/-}$ mice on a C57BL/6J background were purchased at the age of 12 weeks from Janvier (Saint Berthevin, France). One hour prior to the imaging experiments each mouse was anaesthetized by ketamine/xylazine (100 and 15 mg/kg, respectively). After sacrifice, the aorta was flushed *in situ* by transcardiac perfusion with PBS (pH 7.4) through the left ventricle.

After measuring the distance between two marked points with a caliper *in situ*, the left common carotid artery was carefully excised and the *in vivo* stretch was calculated from the length ratio between excised and *in situ* lengths. The artery was subsequently mounted onto the synchrotron-compatible pressure inflation device (Figure 1) and fixed at the *in vivo* axial stretch. Attachment of the artery to the pressure tubes was done with silk wire. In n=1/12 animals the left carotid artery was damaged during the procedure and the right carotid artery was used instead. Once mounted, the tube in which the fresh carotid samples were mounted was immersed in Krebs-Hanseleit solution (in mM: 110.8 NaCl, 5.9 KCl, 25.0 NaHCO3, 1.07 MgSO4, 2.49 CaCl2, 2.33 NaH2PO4 and 11.51 glucose, pH 7.4). The vessel was pre-conditioned with two initial pressure inflation-deflation loops of 0-120 mmHg in 5 minutes. During pressure inflation experiments the pressure was increased quasi-statically by infusion of PBS with a syringe pump. Scans were taken at pressure levels of 0, 10, 20, 30, 40, 50, 70, 90 and 120 mmHg. There was no leakage in the system and pressure was kept constant during the entire scan for all scans of all samples. Propagation-based phase contrast imaging (29, 30) was performed at the X02DA TOMCAT beamline of the Swiss Light Source, Paul Scherrer Institut, Villigen, Switzerland. The Swiss Light Source is a 2.4 GeV synchrotron storage ring, operated in top-up mode with ring current of 400 mA. The X-ray beam at the X02DA TOMCAT beamline is produced by a 2.9 T superbending magnet. Propagation-based phase contrast imaging was performed at 25m source-to-sample distance, 25 cm sample-to-detector distance and at 21 keV. This setup is typically referred to as the "edge-enhancement regime" and facilitates increased contrast at interfaces between different materials(31), in our case between the lamellar and interlamellar layers. For acquiring the tomographic projection data, a scientific CMOS detector (pco.Edge 5.5) was used in combination with a 4x magnifying visible-light optics and a 20 µm thick scintillator (LuAg:Ce). The effective voxel size was 1.625 x 1.625 x 1.625 μm^3. The 3D volumes were then CT-reconstructed with the gridrec algorithm (32). A flowchart summary of all experimental steps is given in supplementary Figure S1.

Image post-processing: automatic 2D segmentation of lamellae

During post-processing the images underwent a fully automated sequence of post-processing steps that were part of a segmentation algorithm that had been specifically designed to extract individual elastic lamellae from the images (Figures 2 and 3). Below is a summarized version of the methodology. A detailed description can be found in the supplementary material. All commands can be found in the image processing toolbox in Matlab R2016b (The Mathworks, USA).

The first intermediate goal was to set all pixels in– and outside the vessel wall to zero. To that end the original image (Figure 2a) was first binarized from greyscale to black and white. Connected items smaller than 10 pixels were removed from the binary image and the image was morphologically closed such that the largest remaining connected item in the image was the vessel wall (Figure 2c). A succession of dilate and erode operations was used to remove erroneous spikes protruding from the vessel wall and a convex hull was computed (Figure 2d). Once the outer convex hull had been identified, its inverse could be subtracted from the original image to eliminate background noise (Figure 2e). A series of Boolean operations was then executed to identify the pixels belonging to the arterial lumen. The inverse of the outer hull was added to the original binary image and the resulting image was subsequently inverted, leaving the inner lumen as the largest single connected item (Figure 2g). The (inverted) outer hull and the inner convex hull were subsequently subtracted from the original greyscale image (Figure 2h).

The second intermediate goal was to process the greyscale image such that it represents the connectivity of the lamellae. In order to expedite the process we first removed the outer half of the aorta (Figure 3b). Once the input image was determined, we set out to find the optimal binary threshold (Figure 3c). Edge gaps with a gap size of 3-5 pixels (Figure 3d, green arrows) were filled in and loose edges (i.e. edges of which either one or both endpoints were not connected to any other edge) were removed (Figure 3d, yellow arrows).

The third intermediate goal was to find the paths that represent the elastic lamellae. We first calculated the coordinates (x_c, y_c) of the geometric center of gravity of the outer convex hull. All pixels

along the vertical axis ($x=x_c$, $y>y_c$) were subsequently set to 0 (Figure 3e, red arrows). Then, a connected graph was calculated in which each elastin line on the image corresponded to an edge in the graph (Figure 3f). The connectivity between these edges was stored in a sparse bi-directional matrix, with two junctions for each intersection between two edges (one junction for each direction). In the next step the starting and ending points of each of the three lamellae were defined as the edges closest to the geometric center that intersected with the pixel column left and right of the zero-column, respectively (Figure 3f, bottom). For each lamella the shortest path along the graph from its start to its end point was then calculated. To every junction in the sparse matrix a weight was attributed that corresponded to the average distance to the eroded hull of both edges belonging to that junction. These weights were subsequently used in a modified version of Dijkstra`s shortest path algorithm (33) (Supplementary Figure S1). The shortest path according to this modified Dijkstra algorithm (Figure 3h) was subsequently back-projected onto the original image (Figure 3i). As a last step, the path was filtered in order to correct for discrepancies that were introduced during the skeletonization step (e.g. the transition from Figure 3c to Figure 3d). For each pixel, the local lamellar thickness was calculated as twice the distance between the curve representing the segmented lamella (corresponding to the local centerline of the lamella, Figure 3i) and the inner lining of the binarized image (corresponding to the local inner curvature of the lamella, innermost pixels of Figure 3c). This local thickness array was used to smooth the lamellar path (Figure 3j). Once the lamella centerline and corresponding local thickness array had been calculated, this information was used to remove the segmented lamella from the original image. This yielded a new input image similar to the one shown in Figure 3b, but now with the second lamella being the innermost lamella (Figure 3k). Steps b to j were repeated, resulting in a segmented second (middle) lamella (Figure 3l). The second lamella was then removed from the original image (Figure 3m) and the outermost lamella was segmented (Figure 3n). Finally the outer lining of the adventitia was segmented from the outer convex hull. In a final step, the resulting adventitial lining was smoothed with a Savitsky-Golay filter and all segmented layers

(outer lining of adventitia and centerline of three lamellae) were back-projected onto the original image (Figure 3o).

Image post-processing: automatic 3D segmentation of lamellae

The 2D procedure as described above was followed for all slices in the geometry, and these were subsequently connected in axial direction in order to form a 3D surface. We skipped 2 out of every 3 axial images, reducing the effective axial resolution to 4.9 μm and resulting in a stack of 75 images per pressure level (representing an axial length of 366 μm). All 2D segmentations in which one of the layers could not be segmented were discarded automatically. The remaining 3D layers were smoothed using built-in functions of the Vascular Modelling Toolkit (VMTK (34).

Image post-processing: quantification of lamellar diameter, length, thickness and straightness

Once the three lamellar layers were segmented (Figure 2, 3), this information was used to quantify how each of the three lamellar layers straightened when pressurized. In order to get the diameter value, a circle was fit through the points of each segmented lamella by minimizing the sum of squared radial deviations. The total lamellar length was calculated based on the centerline of the final segmented path, and a dimensionless straightness parameter was defined for each lamella as the ratio of (i) the perimeter of the best-fitting circle and (ii) the total lamellar length (21). The thickness of the adventitia and of each lamella were derived from the segmentation algorithm. The interlamellar thickness was calculated from the node-to-node distance between lamellar centerlines, from which half the lamellar thickness was subtracted at each side.

Data analysis

We selected 75 images from the center of each stack (starting at the center of the stack, and skipping 2 of every three images in both cranial and caudal axial directions) for each sample and for each pressure level, resulting in a total of 75 x 12 x 9 = 8100 analyzed images from 108 different scans. Since the samples were fixed at their caudal and cranial end by silk wire, we were able to analyze the same

locations along the carotid at every pressure step. Segmented slices were discarded when: (i) the automatic segmentation algorithm ran into numerical error (n=95/8100 slices), (ii) the automatic segmentation algorithm produced a nonsensical result, detected as a lamellar length that was more than 3 standard deviations away from the average value for that pressure level, representing n=944/8100 slices. In total 1039/8100 images were discarded prior to analysis.

Results

Our synchrotron-based experiments resulted in a clear delineation of the centerline of each lamellar layer (Figure 4). This allowed us to construct image-based 3D models of the lamellar micro-structure of the mouse carotid artery at nine different pressure levels (Figure 4g). To the best of our knowledge, these are the first image-based 3D models that include both the layered lamellar structure within the tunica media and the entire thickness of the adventitia along the entire circumference of the vessel. In the second part of our analysis, we quantified the geometry of the micro-structure in order to investigate how the lamellar diameter, length and straightness evolve with increasing pressure (Figure 5). As pressure increased the diameter of the carotid artery experienced a 50% increase, with the outer, adventitial diameter augmenting from 368 μm at zero pressure to 545 μm at a pressure of 120 mmHg (Table 1, Figure 5a). During this process each of the three lamellar layers unfolded and was simultaneously stretched out, as can be seen from the increase in lamellar length (Table 1, Figure 5b) and lamellar straightness (Table 1, Figure 5c). Lamellar length increased quasi-linearly in all three lamellae (Figure 5b). In each of the three lamellar layers the most important increase in lamellar straightness occurred between 0 and 30 mmHg, after which a plateau value of around 95-97 % straightness was reached (Table 1, Figure 5c). The innermost layer was slightly straighter than the other layers at all pressure levels (straightness of 88% at zero pressure and 97% at a pressure of 120 mmHg, Table 1).

The decrease in thickness of the wall was mostly observed in the outer layers (Figure 6). At zero pressure, media and adventitia had a similar thickness (media: 24.7 μm; adventitia: 27.1 μm). At 120 mmHg, the adventitia had reduced its thickness by 50% (13.8 μm) while the media reduced only by 30% (17.3 μm). At all pressure levels the inner lamella was thicker than the outer lamellae, and the outer interlamellar layer was thicker than the inner interlamellar layer. At 120 mmHg, the thickness of the interlamellar layer between the two innermost lamellae had reduced with 20% (from 3.5 μm to 2.8 μm) while the distance between the two outer lamellae was reduced by 28% (from 5.4 μm to 3.9

μm). Over the same pressure range the lamellae reduced in thickness with 36% (L1: 6.6 to 4.2 μm), 27% (L2: 4.4 to 2.9 μm) and 23% (L3: 4.7 to 3.6 μm). All measurements (35) as well as original synchrotron images (36) are accessible from the online repository Zenodo.

Discussion

In this work we present a novel methodology to visualize and model the microstructure of the carotid arterial wall. Using a synchrotron-compatible pressure inflation device, we report, both qualitatively and quantitatively, how the lamellar layers within the tunica media respond to a gradual increase of intraluminal pressure. This allowed us to create a 3D model of the microstructure which, in future work, can be used as the geometrical input for computational biomechanics of the arterial microstructure.

Imaging the micro-structure: a comparison to literature

The greatest advantage of our synchrotron-based technique is that the field of view in our experiments is larger than that of established imaging techniques such as TEM, SEM or MPM. Raspanti *et al.* used SEM to visualize how unpressurized elastic laminae in the human aortic wall form thin sheets spanning hundreds of microns, all of them folding into a regular undulation (17). MPM has been used to examine the structure of collagen and elastin fibers in healthy (37) and diseased (15, 38) human aortas, as well as in pigs (18, 39), rabbits (40, 41), rats (42) and mice (19, 43-45). Several researchers used MPM to visualize how in an unpressurized, undulating state, the adventitial collagen network shows randomly distributed orientations and a high degree of crimping (40, 42) while the collagen bundles progressively unfold and realign along the load direction upon loading, thus explaining the subsequent stiffening of the material's response (41, 46). MPM-based reports on the behavior of arterial lamellae at different pressures are, however, rare. Zoumi *et al.* studied the deformation of collagen and elastin fibers in rabbit aortas and pig coronary arteries under different distension conditions (47). Focusing on collagen rather than elastin fibers, they reported that the portion of the vessel closer to the lumen was affected by the loading more than the region closer to the outer wall. This finding can be explained by the principle of conservation of mass in an incompressible material, and is consistent with our own observations (both in current and previous work (48)). Chow *et al.* reported that the medial elastic fibers in porcine thoracic aortas are much more uniformly distributed than collagen fibers and remain

relatively unchanged due to loading (37). Sugita *et al.* used MPM to claim that the interlamellar layers within the tunica media of the rabbit thoracic aortas straighten at lower intraluminal pressures than the elastic laminae themselves (49). Walton *et al*. were the first to use synchrotron-based phase contrast imaging to scan the full 3D circumference of paraffin-embedded rat carotid arteries (22). They visualized the elastic lamellae of 2 different samples: one fixed at zero pressure, another fixed at a pressure of 110 mmHg. A semi-automatic segmentation algorithm was able to distinguish between media and adventitia, but singular lamellae were not extracted despite being visible on the images. Since two different samples were used and both samples were embedded in paraffin prior to imaging, there was no direct imaging of how lamellae straighten with pressure (22). More recently, Yu *et al.* were the first to visualize how distinct lamellar layers in the mouse carotid artery unfold with pressure (21). Their MPM-based method had limited depth which prevented them from scanning the entire circumference of the vessel. The tunica adventitia was not measured and lamellae were traced at their centerline only (no thickness values included). Nevertheless, their report includes the most detailed data on pressure-inflation of the murine arterial microstructure to date, which is why we used it as a reference in the following sections.

Unfolding, stretching and thinning of lamellar layers with pressure

We observed that lamellar layers unfold in the pressure range between 0 and 30 mmHg. This is in line with earlier findings of Yu *et al.* (21) and with those of Dobrin, who used radiography to measure the deformation of 4 elastic lamellae in the dog carotid artery and found complete lamellar unfolding at a pressure between 25 and 55 mmHg (50). We also found that lamellar layers stretch (i.e. increase in length) from the lowest pressure levels on, even when the lamellae have not yet unfolded (Figure 5b and 5c). This observation contradicts previous histology-based findings, which suggested that lamellae are only stretched once the intraluminal pressure surpasses the diastolic pressure (51). It is, however, in line with the observations of Yu *et al.*, who reported that unfolding and extension of lamellar layers contribute simultaneously to tissue-level deformation (21).

Another observation that is consistent with findings of Yu *et al.* is that the outer interlamellar layer (L23) is slightly thicker than the inner interlamellar layer (L12). The thickness of both interlamellar layers also decreases as pressure increases (Figure 6b, Table 1). Yu *et al.* based their analysis on the distance between lamella centerlines (not taking the lamellar thickness into account). Our segmentation algorithm allowed for a more accurate breakdown of arterial thinning during pressurization: we found that most of the reduction in medial thickness was due to thinning of the lamellae themselves (Figure 6). An important difference between our data and those of Yu *et al.* was found in the evolution of lamellar straightness with pressure. Our synchrotron-based measurements showed that the inner lamellar layer (L1) was slightly straighter than the middle and outer layers (Figure 5c). Yu *et al.,* on the other hand, reported that the inner lamella L1 undergoes a significantly greater undulation than the other layers, especially at lower pressures. They hypothesized that the inner lamella is less straight than the outer lamellae to compensate for the fact that, during pressurization, the inner radius undergoes more deformation than the outer radius (21). In order to explain this discrepancy with our data, several alternative hypotheses can be considered. A first hypothesis is that lamellar straightness is not homogeneously distributed along the circumference. Indeed, when comparing segmentations of the same 2D image (top quadrant of Figure 4c and right quadrant of Figure 4e), it can be seen that in some regions the inner lamella is straighter than the outer lamella, while in other regions the opposite is true. It is therefore possible that a circumferential compensation mechanism takes place within each lamella: as one region of the lamella is straightened with pressure, another is buckled to compensate. An alternative explanation might be that the mechanism proposed by Yu *et al.* is counteracted by the fact that the middle and outer layers are not directly exposed to the luminal pressure (as is the case for L1). If either of these two hypotheses were correct, this would imply that the results of Yu *et al.* (which were based on MPM imaging of only a small arc, not the entire circumference) might have overestimated the undulation of the inner lamellar layer. Alternatively, one might also hypothesize that the presence of the nearby adventitia introduced an artificial waviness by erroneously incorporating adventitial segments into the outer lamella, thus

leading to an overestimation of the undulation of the outer layers in our synchrotron images (e.g. Figure 4b, 4c). Finally, it is also possible that both our method and that of Yu *et al.* yield correct results and the explanation is to be found in inherent differences between the carotid arteries that were used. In future research we aim to directly compare both methods on the same samples in order to determine the reason for these intriguing differences.

Limitations and future work

The final goal of this work is to generate a computational biomechanics model of the arterial wall in which each of the different lamellar layers is modelled separately. We believe that, on the long term, such micro-structural models will be an indispensable step towards a better understanding of how the micro-mechanics within the vessel affect the initiation and propagation of cardiovascular disease. For such a model to be reliable, one needs (i) a 3D geometry allowing us to represent the lamellar and interlamellar layers within the aortic wall and (ii) layer-specific material properties for each of these layers. This study forms a first step towards that goal, but some shortcomings can still be identified:

1) Geometry

The analysis presented here focuses on the left common carotid artery of mice. From an experimental point of view this is the simplest possible geometry since (i) it has only three lamellar layers and (ii) it is a straight segment without side branches. Our custom-built segmentation algorithm takes advantage of this by assuming that the lamellae encounter no interruptions, bifurcations or dead ends. This assumption is known to be incorrect: using SEM, branching of one lamella into two distinct lamellae has been observed (52), as well as direct connections between lamellae (52), interlamellar elastin (10), and a direct connection between elastin and SMCs (10). In future work, we aim to extend our work to other vascular regions such as the thoracic and/or abdominal aorta and to mouse models with known lamellar defects such as Fibulin5 $^{-/-}$ mice (53). This will require a more sophisticated segmentation algorithm that is able to handle the transition or disruption of lamellar layers. Another limitation is that, while we visualized the elastin components within the tunica media with great detail,

the structural elements within the interlamellar layers and the adventitia (fragmentary elastin fibers, smooth muscle cells, collagen fibrils, etc.) could not be resolved. In future work, a hybrid combination of synchrotron imaging with MPM might allow us to overcome this limitation. Our method also assumed that the artery does not buckle axially in curved or tortuous shapes during inflation, since we compared the same slice at different pressure levels. This assumption was not always valid: at the highest pressure levels some arteries did buckle to some extent, a source of error that should be taken into account when interpreting the high pressure results. Another aspect of the segmentation algorithm that can still be improved is its robustness: In total 1039/8100 2D segmentations had to be discarded due to errors in the shortest path detection algorithm. Some of these errors were caused by collapsed arteries at zero or low pressure (which are difficult to segment in an automated way since the shortest path takes a shortcut when opposite sides of the vessel are touching each other). Other errors could be attributed to image artefacts that affected the automatic image processing, resulting in nonsensical “shortest paths”. Given the very detailed axial (inter-slice) resolution of the synchrotron scans, this limitation can be accounted for as long as the total dataset is sufficiently large to allow for automated skipping of the erroneously segmented slices. We are convinced that future improvements in synchrotron image quality and post-processing techniques (as incremental as they may be) will further improve the accuracy of our results.

2) Material properties

In this work we present a novel segmentation algorithm that allows us to describe the undulating behavior within different lamellar layers of the carotid artery wall. We did not, however, use our pressure-inflation data to estimate the material properties of each individual lamellar and interlamellar layer. It is important to keep in mind that all layers are subjected to the same intraluminal pressure at each quasi-static scan, and any estimate of the material properties should model the interaction between layers, which consist of different constituents (i.e. simply analyzing the pressure-diameter relationship does not suffice)(45). In future work we aim to include a load cell to measure

the axial force exerted on the aorta during inflation to enable such parameter fitting. We are also working on an alternative approach based on isogeometric analysis in order to estimate the material properties.

Conclusions

In this manuscript we present (i) a synchrotron-compatible experimental setup that allows for pressure-inflation experiments on a mouse artery and (ii) an automated segmentation algorithm that allows for geometrical modelling of distinct lamellar layers. Applying our methodology on the carotid artery of a mouse (3 lamellar layers, no side branches), we found that all lamellae are stretched during unfolding, and that the three lamellar layers are similar in straightness when the entire circumference is taken into account. We believe that, in the long term, the results presented in this work can be the first step towards a breakthrough in micro-structural computational biomechanics of the arterial wall – and thus lead to a better understanding of how the micro-structure affects the initiation and propagation of cardiovascular disease.

Author Contributions

BT participated in the design of the study, co-designed the pressure inflation device, participated in the imaging experiments, participated in the data analysis, co-developed the segmentation code and drafted the manuscript; MF participated in the imaging experiments and co-developed the segmentation code; GoLo helped designing the pressure inflation device and coordinated the imaging experiments; LA and GeLo participated in the imaging experiments and helped with the data analysis; PS participated in the design of the study and critically revised the manuscript; NS conceived of the study and participated in its design. All authors gave final approval for publication and agree to be held accountable for the work performed therein.

Acknowledgments

We would like to thank Stéphane Bigler (EPFL) and Thomas Steigmeier (PSI) for their assistance with the design, manufacturing and maintenance of the pressure inflation device, and Mira Puthettu (EPFL) for her help designing the first prototype. We also thank Heleen Fehervary (KU Leuven) and Georges Samaras (EPFL) for their help during the scans, and Fabiana Fraga-Silva (EPFL) who prepared and mounted the arteries prior to scanning. We acknowledge the Paul Scherrer Institut, Villigen, Switzerland for provision of synchrotron radiation beam time at the TOMCAT beamline X02DA of the Swiss Light Source.

Data Accessibility

All data can be downloaded from Zenodo.org. One dataset contains a matlab file with all primary numerical data used to produce the graphs and tables. This dataset also contains 2D segmentations in .tif format (doi: 10.5281/zenodo.2593708). Another dataset contains the original synchrotron images in .tif format (doi: 10.5281/zenodo.1462952). Electronic supplementary material to the manuscript, including a detailed methods section and an additional results section describing

the observed (lack of) differences between WT and ApoE$^{-/-}$ mice, is available online at rs.figshare.com (https://dx.doi.org/10.6084/m9.figshare.c.4536683).

Ethics

All procedures were approved by the intercantonal Ethical Committee of Cantons Vaud and Aarau, Switzerland (EC VD3161.a) and performed according to the guidelines from Directive 2010/63/EU of the European Parliament on the protection of animals used for scientific purposes.

Funding Statement

This project was funded by a research grant from the Swiss National Science Foundation (SNSF, grant CR23I2_163370) and by a research grant from the Research Fund Flanders (FWO, grant G086917N). Gerlinde Logghe and Bram Trachet are supported by a scholarship of the Research Fund Flanders (FWO, grants 1S26117N and 12A5816N).

References

1. Voytik-Harbin SL, Roeder BA, Sturgis JE, Kokini K, Robinson JP. Simultaneous Mechanical Loading and Confocal Reflection Microscopy for Three-Dimensional Microbiomechanical Analysis of Biomaterials and Tissue Constructs. Microscopy and Microanalysis. 2003;9(1):74-85.
2. Hill MR, Duan X, Gibson GA, Watkins S, Robertson AM. A theoretical and non-destructive experimental approach for direct inclusion of measured collagen orientation and recruitment into mechanical models of the artery wall. J Biomech. 2012;45(5):762-71.
3. Sacks MS, Sun W. Multiaxial Mechanical Behavior of Biological Materials. Annu Rev Biomed Eng. 2003;5(1):251-84.
4. Humphrey JD, Taylor CA. Intracranial and abdominal aortic aneurysms: Similarities, differences, and need for a new class of computational models. Annu Rev Biomed Eng. 2008;10:221-46.
5. Chen H, Slipchenko MN, Liu Y, Zhao X, Cheng J-X, Lanir Y, et al. Biaxial deformation of collagen and elastin fibers in coronary adventitia. J Appl Physiol. 2013;115(11):1683-93.
6. Gleason RL, Gray SP, Wilson E, Humphrey JD. A Multiaxial Computer-Controlled Organ Culture and Biomechanical Device for Mouse Carotid Arteries. J Biomech Eng. 2005;126(6):787-95.
7. Holzapfel GA, Sommer G, Gasser CT, Regitnig P. Determination of layer-specific mechanical properties of human coronary arteries with nonatherosclerotic intimal thickening and related constitutive modeling. American Journal of Physiology-Heart and Circulatory Physiology. 2005;289(5):H2048-H58.
8. Teng Z, Tang D, Zheng J, Woodard PK, Hoffman AH. An experimental study on the ultimate strength of the adventitia and media of human atherosclerotic carotid arteries in circumferential and axial directions. J Biomech. 2009;42(15):2535-9.

9. Clark JM, Glagov S. Transmural organization of the arterial media. The lamellar unit revisited. Arterioscler Thromb Vac Biol. 1985;5(1):19-34.
10. Dingemans KP, Teeling P, Lagendijk JH, Becker AE. Extracellular matrix of the human aortic media: an ultrastructural histochemical and immunohistochemical study of the adult aortic media. Anat Rec. 2000;258(1):1-14.
11. Wolinsky H. Response of the Rat Aortic Media to Hypertension. Morphological and Chemical Studies. 1970;26(4):507-22.
12. Chen H, Liu Y, Slipchenko Mikhail N, Zhao X, Cheng J-X, Kassab Ghassan S. The Layered Structure of Coronary Adventitia under Mechanical Load. Biophys J. 2011;101(11):2555-62.
13. Gasser TC, Ogden RW, Holzapfel GA. Hyperelastic modelling of arterial layers with distributed collagen fibre orientations. Journal of The Royal Society Interface. 2006;3(6):15-35.
14. Zulliger MA, Fridez P, Hayashi K, Stergiopulos N. A strain energy function for arteries accounting for wall composition and structure. J Biomech. 2004;37(7):989-1000.
15. Niestrawska JA, Viertler C, Regitnig P, Cohnert TU, Sommer G, Holzapfel GA. Microstructure and mechanics of healthy and aneurysmatic abdominal aortas: experimental analysis and modelling. Journal of The Royal Society Interface. 2016;13(124):20160620.
16. Wolinsky H, Glagov S. Comparison of Abdominal and Thoracic Aortic Medial Structure in Mammals. Circ Res. 1969;25(6):677-86.
17. Raspanti M, Protasoni M, Manelli A, Guizzardi S, Mantovani V, Sala A. The extracellular matrix of the human aortic wall: Ultrastructural observations by FEG-SEM and by tapping-mode AFM. Micron. 2006;37(1):81-6.
18. Cavinato C, Helfenstein-Didier C, Olivier T, du Roscoat SR, Laroche N, Badel P. Biaxial loading of arterial tissues with 3D in situ observations of adventitia fibrous microstructure: A method coupling multi-photon confocal microscopy and bulge inflation test. Journal of the Mechanical Behavior of Biomedical Materials. 2017;74(Supplement C):488-98.
19. Wan W, Dixon JB, Gleason Rudolph L. Constitutive Modeling of Mouse Carotid Arteries Using Experimentally Measured Microstructural Parameters. Biophys J. 2012;102(12):2916-25.
20. Haskett D, Doyle JJ, Gard C, Chen H, Ball C, Estabrook MA, et al. Altered tissue behavior of a non-aneurysmal descending thoracic aorta in the mouse model of Marfan syndrome. Cell Tissue Res. 2012;347(1):267-77.
21. Yu X, Turcotte R, Seta F, Zhang Y. Micromechanics of elastic lamellae: unravelling the role of structural inhomogeneity in multi-scale arterial mechanics. Journal of The Royal Society Interface. 2018;15(147).
22. Walton LA, Bradley RS, Withers PJ, Newton VL, Watson REB, Austin C, et al. Morphological Characterisation of Unstained and Intact Tissue Micro-architecture by X-ray Computed Micro- and Nano-Tomography. Scientific Reports. 2015;5:10074.
23. Wilkins SW, Nesterets YI, Gureyev TE, Mayo SC, Pogany A, Stevenson AW. On the evolution and relative merits of hard X-ray phase-contrast imaging methods. Philosophical Transactions of the Royal Society A: Mathematical, Physical and Engineering Sciences. 2014;372(2010):20130021.
24. Trachet B, Piersigilli A, Fraga-Silva RA, Aslanidou L, Astolfo A, Stampanoni MFM, et al. Ascending aortic aneurysm in angiotensin II infused mice: Formation, progression and the role of focal dissections. Arterioscler Thromb Vac Biol. 2016;36:673-81.
25. Trachet B, Aslanidou L, Piersigilli A, Fraga-Silva RA, Sordet-Dessimoz J, Villanueva-Perez P, et al. Angiotensin II infusion into ApoE-/- mice: a model for aortic dissection rather than abdominal aortic aneurysm? Cardiovasc Res. 2017;113(10):1230-42.
26. Trachet B, Fraga-Silva RA, Piersigilli A, Tedgui A, Sordet-Dessimoz J, Astolfo A, et al. Dissecting abdominal aortic aneurysm in ang II-infused mice: suprarenal branch ruptures and apparent luminal dilatation. Cardiovasc Res. 2015;105(2):213-22.
27. Lareyre F, Clément M, Raffort J, Pohlod S, Patel M, Esposito B, et al. TGFβ (Transforming Growth Factor-β) Blockade Induces a Human-Like Disease in a Nondissecting Mouse Model of Abdominal Aortic Aneurysm. Arterioscler Thromb Vac Biol. 2017.

28. Logghe G, Trachet B, Aslanidou L, Villaneuva-Perez P, De Backer J, Stergiopulos N, et al. Propagation-based phase-contrast synchrotron imaging of aortic dissection in mice: from individual elastic lamella to 3D analysis. Scientific Reports. 2018;8(1):2223.
29. Snigirev A, Snigireva I, Kohn V, Kuznetsov S, Schelokov I. On the possibilities of x-ray phase contrast microimaging by coherent high-energy synchrotron radiation. Rev Sci Instrum. 1995;66(12):5486-92.
30. Wilkins SW, Gureyev TE, Gao D, Pogany A, Stevenson AW. Phase-contrast imaging using polychromatic hard X-rays. Nature. 1996;384:335.
31. Nugent KA. Coherent methods in the X-ray sciences. Advances in Physics. 2010;59(1):1-99.
32. Marone F, Stampanoni M. Regridding reconstruction algorithm for real-time tomographic imaging. Journal of Synchrotron Radiation. 2012;19(6):1029-37.
33. Dijkstra EW. A note on two problems in connexion with graphs. Numerische Mathematik. 1959;1(1):269-71.
34. Antiga L, Piccinelli M, Botti L, Ene-Iordache B, Remuzzi A, Steinman DA. An image-based modeling framework for patient-specific computational hemodynamics. Med Biol Eng Comput. 2008;46(11):1097.
35. Trachet B, Ferraro M, Lovric G, Aslanidou L, Logghe G, Segers P, et al. Synchrotron-based visualization and segmentation of elastic lamellae in the mouse carotid artery during quasi-static pressure inflation: 2D segmentations [Data set]. Zenodo. 2019; Available from: http://doi.org/10.5281/zenodo.2593708.
36. Trachet B, Ferraro M, Lovric G, Aslanidou L, Logghe G, Segers P, et al. Synchrotron-based visualization and segmentation of elastic lamellae in the mouse carotid artery during quasi-static pressure inflation: dataset (Version 1.0.0) [Data set]. Zenodo. 2018; Available from: http://doi.org/10.5281/zenodo.1462952.
37. Chow M-J, Turcotte R, Lin Charles P, Zhang Y. Arterial Extracellular Matrix: A Mechanobiological Study of the Contributions and Interactions of Elastin and Collagen. Biophys J. 2014;106(12):2684-92.
38. Tsamis A, Phillippi JA, Koch RG, Pasta S, D'Amore A, Watkins SC, et al. Fiber micro-architecture in the longitudinal-radial and circumferential-radial planes of ascending thoracic aortic aneurysm media. J Biomech. 2013;46(16):2787-94.
39. Zeinali-Davarani S, Wang Y, Chow M-J, Turcotte R, Zhang Y. Contribution of Collagen Fiber Undulation to Regional Biomechanical Properties Along Porcine Thoracic Aorta. J Biomech Eng. 2015;137(5):051001--10.
40. Rezakhaniha R, Agianniotis A, Schrauwen JTC, Griffa A, Sage D, Bouten CVC, et al. Experimental investigation of collagen waviness and orientation in the arterial adventitia using confocal laser scanning microscopy. Biomech Model Mechanobiol. 2012;11(3):461-73.
41. Krasny W, Morin C, Magoariec H, Avril S. A comprehensive study of layer-specific morphological changes in the microstructure of carotid arteries under uniaxial load. Acta Biomater. 2017;57(Supplement C):342-51.
42. O'Connell MK, Murthy S, Phan S, Xu C, Buchanan J, Spilker R, et al. The three-dimensional micro- and nanostructure of the aortic medial lamellar unit measured using 3D confocal and electron microscopy imaging. Matrix Biol. 2008;27(3):171-81.
43. van Zandvoort M, Engels W, Douma K, Beckers L, oude Egbrink M, Daemen M, et al. Two-Photon Microscopy for Imaging of the (Atherosclerotic) Vascular Wall: A Proof of Concept Study. J Vasc Res. 2004;41(1):54-63.
44. López-Guimet J, Andilla J, Loza-Alvarez P, Egea G. High-Resolution Morphological Approach to Analyse Elastic Laminae Injuries of the Ascending Aorta in a Murine Model of Marfan Syndrome. Scientific Reports. 2017;7:1505.
45. Clark TE, Lillie MA, Vogl AW, Gosline JM, Shadwick RE. Mechanical contribution of lamellar and interlamellar elastin along the mouse aorta. J Biomech. 2015;48(13):3599-605.

46. Schrauwen JTC, Vilanova A, Rezakhaniha R, Stergiopulos N, van de Vosse FN, Bovendeerd PHM. A method for the quantification of the pressure dependent 3D collagen configuration in the arterial adventitia. J Struct Biol. 2012;180(2):335-42.
47. Zoumi A, Lu X, Kassab GS, Tromberg BJ. Imaging Coronary Artery Microstructure Using Second-Harmonic and Two-Photon Fluorescence Microscopy. Biophys J. 2004;87(4):2778-86.
48. Segers P, Rabben IS, De Backer J, De Sutter J, Gillebert CT, Van Bortel L, et al. Functional analysis of the common carotid artery: relative distension differences over the vessel wall measured in vivo. J Hypertens. 2004;22(5):973-81.
49. Sugita S, Matsumoto T. Multiphoton microscopy observations of 3D elastin and collagen fiber microstructure changes during pressurization in aortic media. Biomech Model Mechanobiol. 2017;16(3):763-73.
50. Dobrin PB. Distribution of lamellar deformations: implications for properties of the arterial media. Hypertension. 1999;33(3):806-10.
51. Sokolis DP, Kefaloyannis EM, Kouloukoussa M, Marinos E, Boudoulas H, Karayannacos PE. A structural basis for the aortic stress–strain relation in uniaxial tension. J Biomech. 2006;39(9):1651-62.
52. Berry CL, Looker T, Germain J. The growth and development of the rat aorta. I. Morphological aspects. J Anat. 1972;113(Pt 1):1-16.
53. Yanagisawa H, Davis EC, Starcher BC, Ouchi T, Yanagisawa M, Richardson JA, et al. Fibulin-5 is an elastin-binding protein essential for elastic fibre development in vivo. Nature. 2002;415(6868):168-71.

Tables

Pressure (mmHg)		0	10	20	30	40	50	70	90	120
Diameter (μm)	**L1**	270	279	321	344	362	382	416	446	485
	L2	289	296	338	361	378	398	432	459	498
	L3	309	317	358	382	399	418	450	476	514
	Adv	368	371	406	427	444	459	488	510	545
Length (μm)	**L1**	962	966	1072	1133	1189	1246	1350	1443	1574
	L2	1036	1013	1128	1191	1246	1307	1416	1508	1648
	L3	1122	1093	1209	1272	1325	1385	1492	1580	1705
Straightness (μm/ μm)	**L1**	0.88	0.91	0.94	0.95	0.96	0.96	0.97	0.97	0.97
	L2	0.87	0.92	0.94	0.95	0.95	0.96	0.96	0.96	0.95
	L3	0.86	0.91	0.93	0.94	0.95	0.95	0.95	0.95	0.95
Thickness (μm)	**L1**	6.6	6.2	5.9	5.9	5.8	5.6	6.0	5.4	4.2
	L2	4.4	4.2	4.3	4.6	4.5	4.0	3.5	3.2	2.9
	L3	4.7	5.2	5.3	5.5	5.6	5.3	4.8	4.3	3.6
	L12	3.5	2.7	2.8	2.6	2.7	2.7	2.8	2.8	2.8
	L23	5.4	4.7	4.8	4.9	4.9	4.7	4.6	4.3	3.9
	Media	24.7	23.0	23.0	23.5	23.5	22.3	21.7	20.0	17.3
	Adv	27.1	23.9	20.6	19.6	19.3	18.1	16.2	14.9	13.8

Table 1. Quantitative assessment of lamellar diameter, length, straightness and thickness as a function of increasing pressure. L1: inner lamellar layer, L2: middle lamellar layer, L3: outer lamellar layer, Adv: Adventitita, L12 and L23: interlamellar layers. All data are reported as mean values over n=12 mice (n=6 ApoE $^{-/-}$ and n=6 WT mice).

Figures

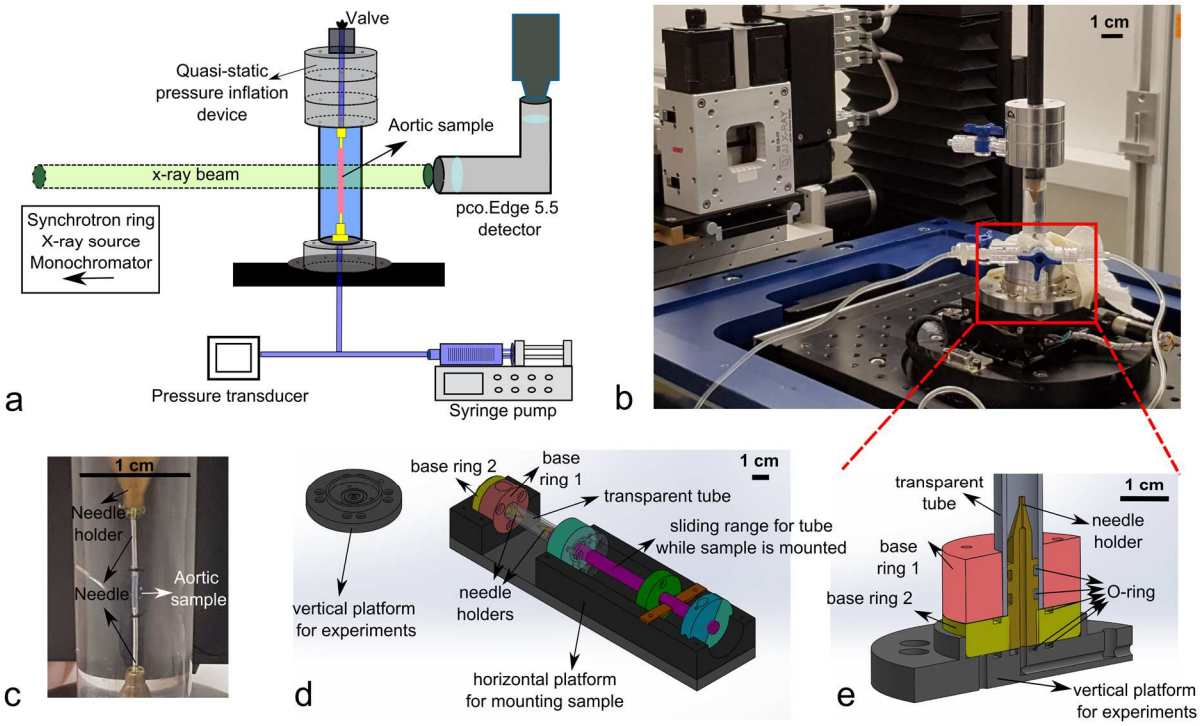

Figure 1. Experimental setup. **a.** Sketch of the pressure-inflation device. **b.** The setup mounted in vertical position, at the Tomcat beam line of the Swiss Light Source. **c**. Left common carotid artery during pressurization. **d.** 3D sketch of the device in horizontal position. The transparent tube can be moved back, to allow the experimenter to mount the sample on the needles. **e**. 3D sketch of the device in vertical position. The view is cut half-way to show the O-rings that seal the pressure inside.

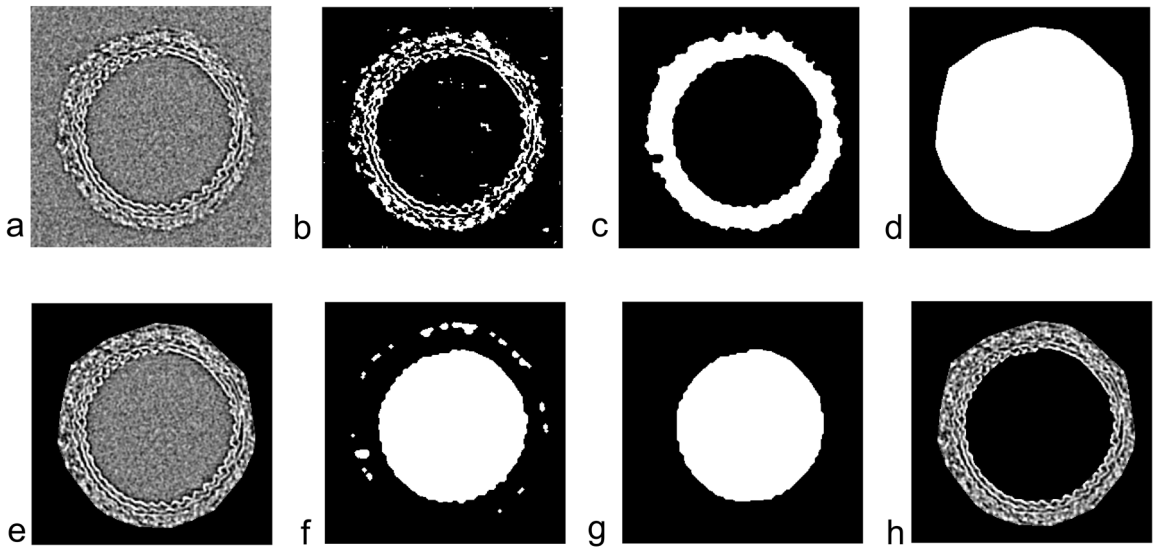

Figure 2. Pre-processing of images for automatic segmentation. **a.** Original image. **b.** After automatic thresholding. **c**. Initial approximation of wall. **d.** Outer convex hull. **e.** Subtract outer background. **f.** Determine inner surface. **g.** Inner convex hull. **h.** Subtract inner background.

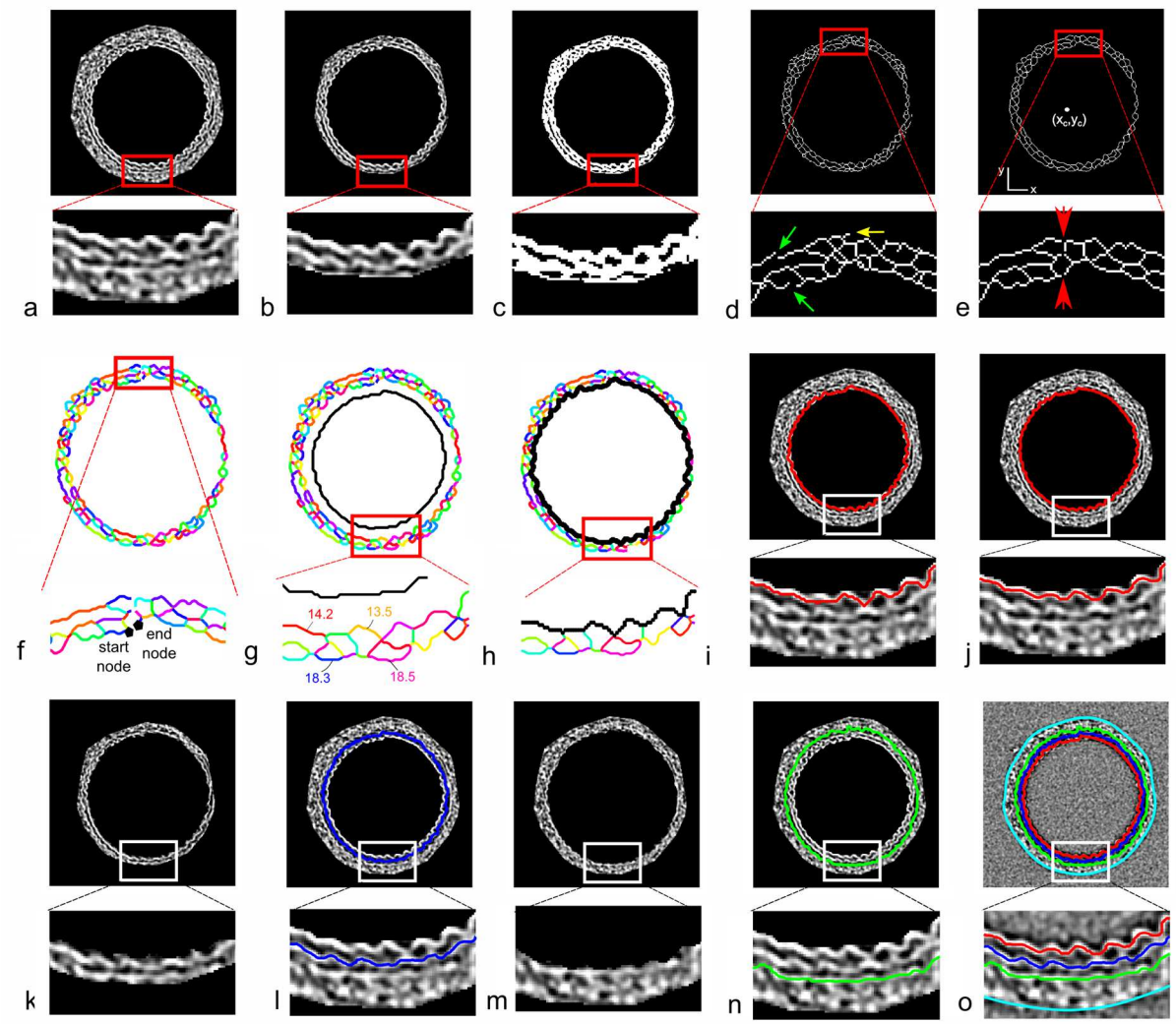

Figure 3. Automatic segmentation of aortic lamellae. **a.** Load pre-processed image (see Figure 2). **b.** Remove outer layers to expedite the segmentation procedure. **c.** Binarize with optimal binary threshold. **d.** Skeletonize. **e.** Fill edge gaps and remove loose edges. Remove pixels at $x=x_c$, where x_c is the x-coordinate of the geometric center of gravity of the outer convex hull. **f**. Compute a graph that consists of junctions and vertices. Each vertex is represented in a different color. Define a start node and an end node on the inner lamella, left and right of y=0. **g**. Attributed a weight to each junction, corresponding to the mean distance of the nodes on the two vertices it connects to the shrunk inner convex hull (black line). **h**. Calculate the inner lamella using a modified version of Dijkstra`s algorithm (Figure 2c). The lamella is the shortest weighted path from start node to end node. **i.** Project segmented lamellae back onto the original image. **j.** Calculate lamellar thickness and use it to smooth lamellar centerline. **k.** Remove segmented inner lamella from the original image. Remove outer half of the aorta to expedite the segmentation procedure. **l.** Repeat the entire procedure (b-j) to find the second lamella. **m.** Remove the two segmented lamellae from the original image. Note that the outer half is not removed in this third iteration to avoid that the wall becomes too thin. **n.** Repeat the entire procedure (b-j) to find the third lamella. **o.** Segment adventitia from outer convex hull and project all segmented layers back onto the original image.

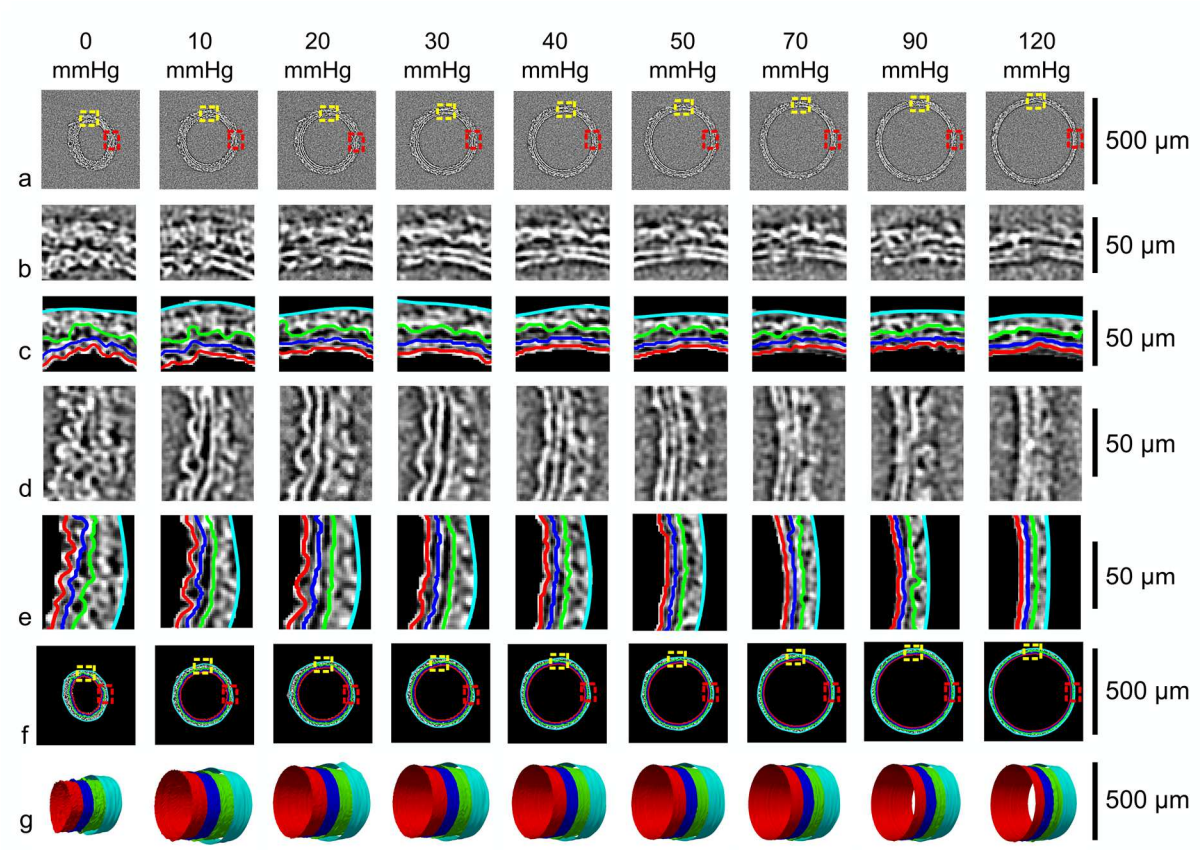

Figure 4. Final results of quasi-static imaging and automatic segmentation at incremental pressure levels. **a,b,d.** 2D images of left common-carotid artery as it is inflated from 0 to 120 mmHg. **c,e,f.** 2D segmentations of elastic lamellae. **g**. 3D segmentations of elastic lamellae. Images correspond to an axial length of 366 micrometer (the equivalent of 75 segmented 2D slices, segmenting 1 of every 3 slices). Red: inner lamella centerline, blue: middle lamella centerline, green: outer lamella centerline, cyan: adventitia outer lining. Note that the yellow and red dotted boxes in panels a and f correspond to the zoomed images in panels b-e.

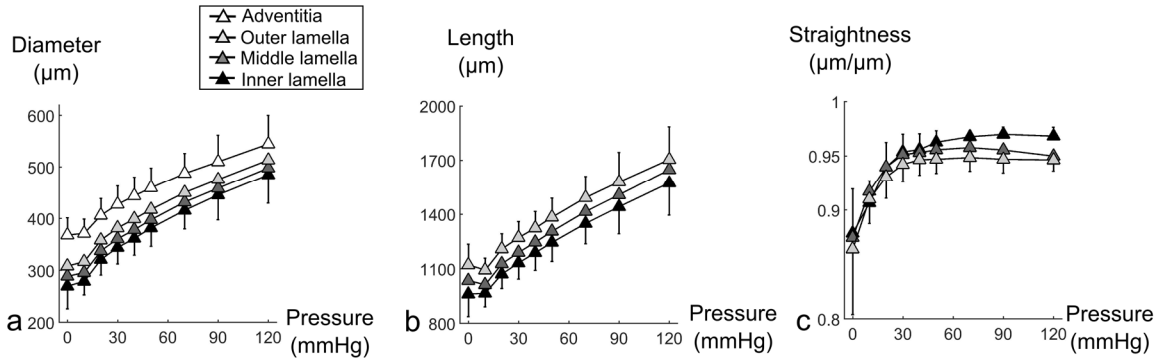

Figure 5. Diameters (**a**), total lamellar length (**b**) and straightness (**c**) for increasing quasi-static pressure levels.

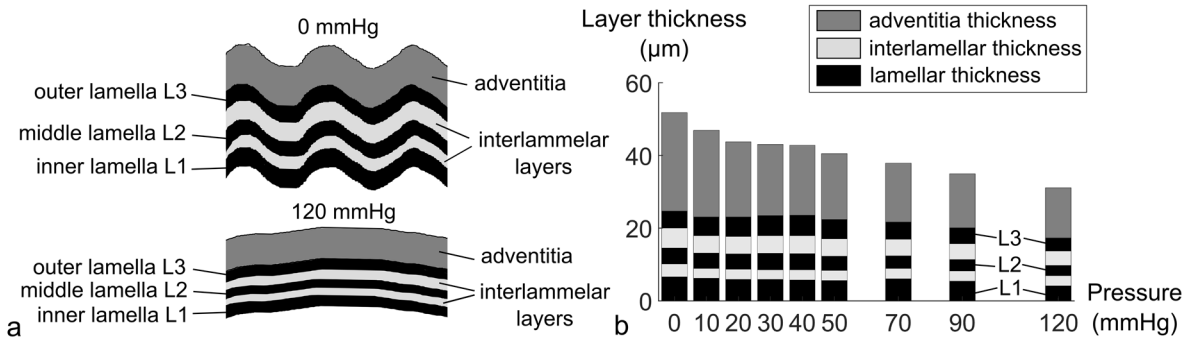

Figure 6. Evolution of lamellar, interlamellar and adventitial thickness with increasing pressure. **a.** Schematic depiction of different layers within the arterial wall at zero pressure (top) and at 120 mmHg (bottom). **b.** Thinning of layer thickness with increasing pressure.

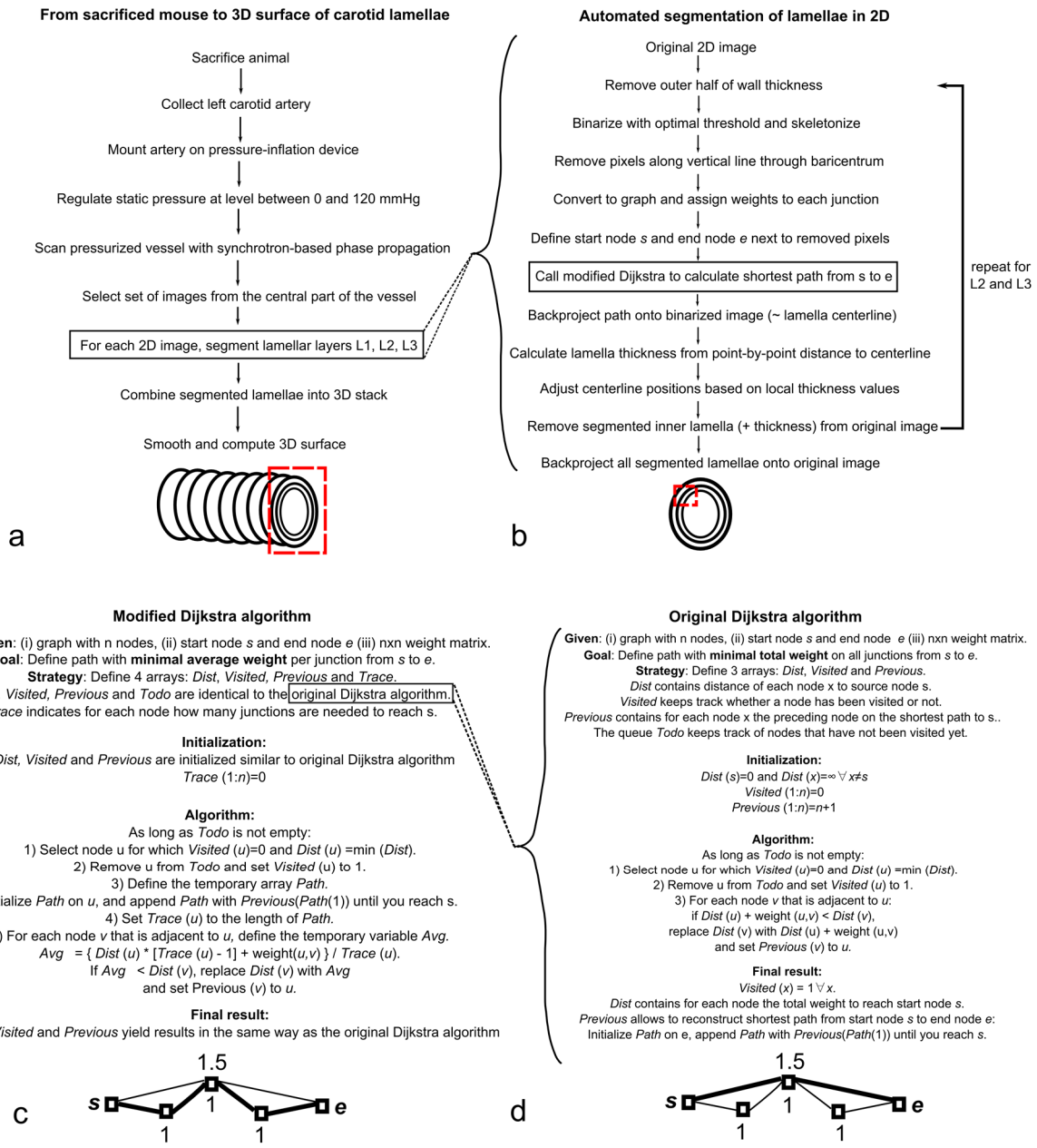

Figure S1. Flow chart of the different experimental and computational steps. **a.** Experimental procedure. **b.** Segmentation procedure. **c.** Modified Dijkstra algorithm. Dijkstra's original shortest path algorithm (32) (**d**) was modified such that the shortest path is the one indicated in bold on the figure. Since weights are assigned based on the distance of the vertices belonging to each junction to the shrunk convex hull, the inner lamella is the lamella with minimal average weight on its junctions (panel **c**) and not the lamella with the minimal total weight (panel **d**). Red rectangles in panels **a** and **b** indicate the focus region of the next panel.

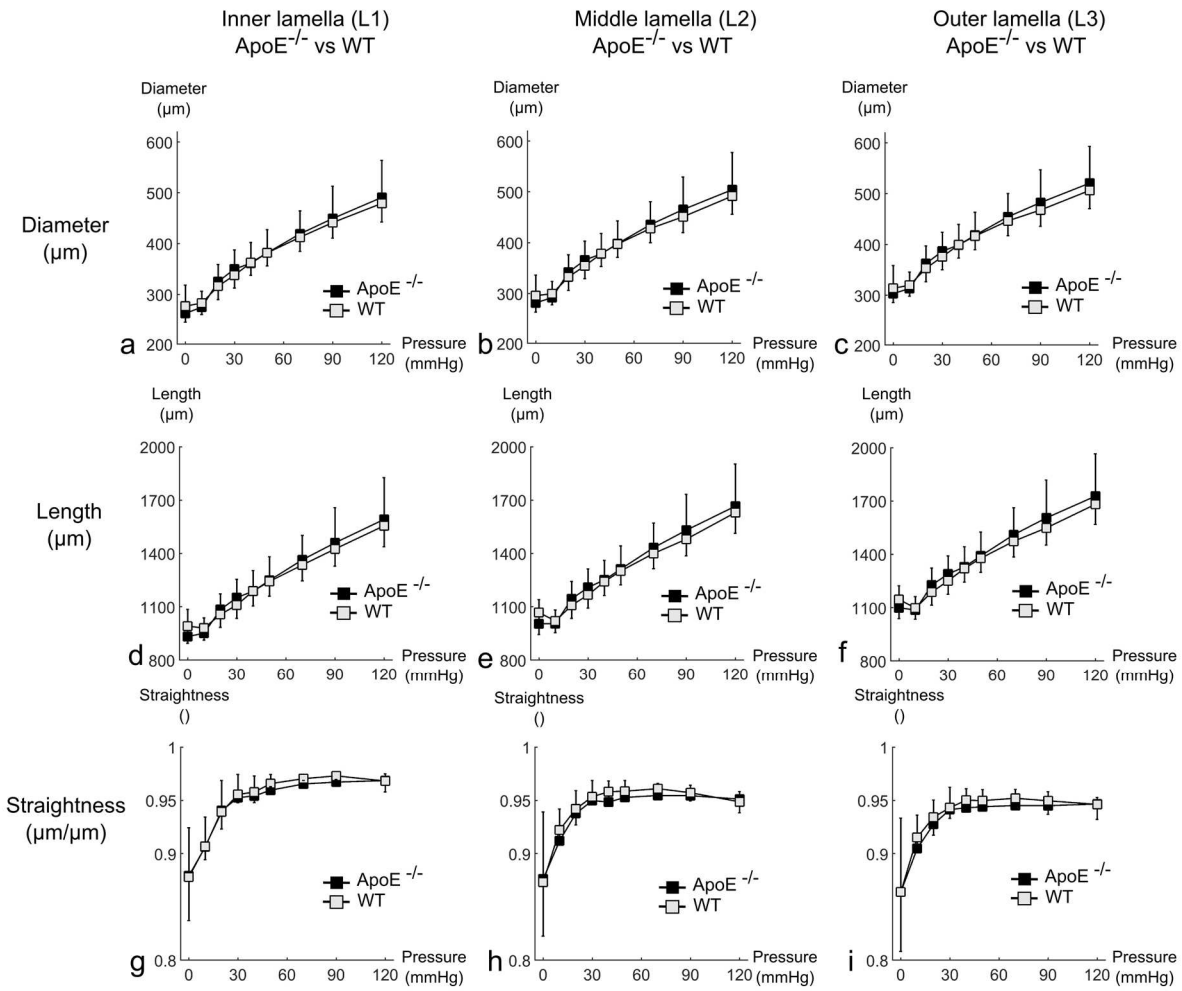

Figure S2. Differences between ApoE$^{-/-}$ and WT mice in diameter (a-c), lamellar length (d-f) and straightness (g-i). Data are shown for the inner lamella L1 (a,d,g), the middle lamella L2 (b,e,h) and the outer lamella L3 (c,f,i).